Resonant and nonresonant spin filtering in bismuthene-silicon cowrie shell-like nanostructures

Alireza Saffarzadeh [1,2] and George Kirczenow [1,*]

[1]*Department of Physics, Simon Fraser University, Burnaby, British Columbia, Canada V5A 1S6*
[2]*Department of Physics, Payame Noor University, P.O. Box 19395-3697 Tehran, Iran*

We predict that two distinct strong spin filtering mechanisms in two-terminal geometries at zero magnetic field should be exhibited by bismuthene-silicon nanostructures with cowrie shell-like geometries. One of these is resonant spin filtering where a peak in resonant transmission of one spin species through the nanostructure coincides with an antiresonant transmission dip for the other spin species. The second is strong nonresonant spin filtering where nonresonant transmission of one spin species is much weaker than that of the other spin species. These mechanisms arise from localized electronic states associated with strong disorder and strong spin-orbit coupling in the bismuthene and differ fundamentally from edge state-related spin filtering and from the spin Hall effect. Our density functional theory (DFT)-based simulations suggest that such cowrie shell-like nanostructures can form by spontaneous folding of bismuthene-silicon bilayer domes with armchair edges.

I. INTRODUCTION

Two-dimensional topological insulators (2DTIs) exhibit a quantum spin Hall (QSH) effect when the Fermi level is located in the bulk band gap [1–10]. In the QSH effect, the electric current is carried by spin-polarized electrons with opposite spin orientations at the opposite edges of the sample. While the 2D QSH systems considered previously had been planar [7–10], we have recently proposed [11] that *curved* 2D QSH systems are possible and that the spatial orientations of the spin polarizations of their edge states can be controlled by appropriately tailoring the curved sample geometry. As an example, we considered an approximately hemispherical bismuthene dome, stabilized by an adsorbed silicon mono-layer and hydrogen atoms [11]. Our density functional theory (DFT) and tight-binding calculations showed [11] that (unlike for planar 2D QSH devices) it is possible to bring the spin polarizations of electron edge states traveling along opposite edges of this dome into parallel alignment and thus to realize a nearly perfect two-terminal spin filter operating in the absence of magnetic fields.

In the bismuthene dome studied in Ref. [11], the bismuth atoms formed hexagons and pentagons, each bismuth atom having three nearest neighbors. The edge of the dome had a well-ordered zigzag structure. These qualitative features were retained when the geometry of the structure was relaxed, optimizing its energy within DFT.

Here we shall consider spin filtering by curved bismuthene nanostructures that are much less regular. They were formed by starting with a spherical dome of bismuthene, coated on its concave side with a monolayer of silicon atoms whose edge was passivated with hydrogen, as shown in Fig. 1(a). Notice that the edge of the dome in Fig. 1(a) has an armchair

structure. Domes with such initial geometries were relaxed by means of density functional theory (DFT) computer simulations. The DFT calculations reported throughout this paper were carried out with the GAUSSIAN 16 package using the B3PW91 functional and Lanl2DZ effective core potential and basis sets [12]. The electronic energy and ionic forces of our optimized geometries were converged within 10^{-5} eV and 0.0008 eV/Å, respectively. Unlike the dome with the zigzag edge in Ref. [11], the geometries of domes with armchair edges changed qualitatively upon relaxation as shown for the
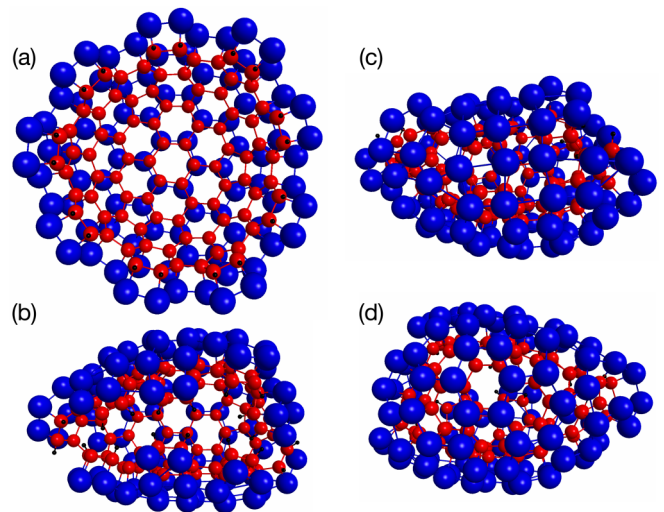
FIG. 1. [(b)–(d)] Three views of a $Bi_{90}Si_{90}H_{18}$ nanostructure produced by relaxing a spherical bismuthene dome (a) with 90 bismuth atoms (blue), a silicon atom (red) bound to each bismuth atom and a hydrogen atom (black) passivating each silicon edge atom. The edge of the starting structure (a) was of the armchair type. Image prepared using Macmolplt software [34].

$Bi_{90}Si_{90}H_{18}$ nanostructure in Figs. 1(b)–1(d). As shown in Fig. 1(b), after relaxation the upper and lower edges of the dome of Fig. 1(a) have pulled together to produce a cowrie shell-like structure. The surface of the nanostructure that is furthest from these edges is shown in Fig. 1(d). There the bismuth atoms have retained three bismuth nearest neighbors and somewhat distorted bismuthene hexagons remain visible. However, closer to the edges the atomic structure is qualitatively different as shown in Fig. 1(c). Strong structural disorder is present there in the form of variations of the Bi-Bi bond lengths and variable Bi atomic coordination numbers, many of the bismuth atoms having four nearest neighbors instead of three. Nevertheless, exactly one silicon atom remains bound to each bismuth atom and all of the silicon atoms remain in the interior of the cowrie shell-like structure.

Because of this more complex atomic geometry, the edge-state mechanism responsible for spin filtering in the simpler structure discussed in Ref. [11] does not apply to nanostructures of the kind shown in Figs. 1(b)–1(d). However, it will be shown below that spin filtering with drain current spin polarizations greater than 95% can be achieved in two-terminal geometries in these systems at zero magnetic field due to spin-selective resonant and nonresonant scattering processes.

In this article we shall present our results for the $Bi_{90}Si_{90}H_{18}$ structure shown in Figs. 1(b)–1(d). However, we have also studied a somewhat larger $Bi_{108}Si_{108}H_{18}$ cowrie shell-like structure, also obtained by relaxing an armchair-edged dome, and found qualitatively similar results.

While nanotubes and fullerene-like nanoparticles based on graphene and on many inorganic compounds with lamellar two-dimensional structure have been synthesized [13], whether *curved* bismuthene-silicon bilayers such as those proposed above can be realized experimentally is unknown at present. In this regard, it is encouraging that bismuth nanotubes have already been synthesized [14–21]. One potential approach to realizing curved bismuthene-silicon bilayers might be to deposit a monolayer of bismuth atoms on a silicon fullerene. However, at the present time silicon fullerenes have yet to be made in the laboratory, although a Si_{20} silafullerane with an endohedral chloride ion has been synthesized [22]. Another possibility may be to deposit a bismuth monolayer on a silicon nanoparticle; silicon nanoparticles with crystalline cores but amorphous outer shells and ranging in size from 2 to 64 nm have been synthesized [23,24].

The remainder of this paper is organized as follows: Our optimized tight-binding model of the cowrie shell-like nanostructure is described in Sec. II; the model parameters are presented in Tables I–V. The Landauer theory used in our transport calculations is described in Sec. III. The results of our spin transport calculations and their interpretation are presented in Sec. IV. Our conclusions are summarized in Sec. V.

II. OPTIMIZED TIGHT-BINDING MODEL

The tight-binding model that we employ here is an extension of the model of curved bismuthene with an adsorbed silicon monolayer that was proposed in Ref. [11]. The latter model was itself based on a previously developed tight-binding model of planar bismuthene on SiC [25].

TABLE I. The onsite orbital matrix elements $H^0_{\alpha,\alpha'}$ for atom i in Eq. (2). Here $\hat{r} = (a, b, c)$ is the unit vector in direction from the nucleus of Si atom bound to Bi atom i towards the nucleus of Bi atom i. The parameter values are $E_s = -10.22$ eV and $E_r = -6.0$ eV.

$H^0_{\alpha,\alpha'}$	$6s'$	$6p'_x$	$6p'_y$	$6p'_z$
$6s$	E_s	0	0	0
$6p_x$	0	$a^2 E_r$	$ab E_r$	$ac E_r$
$6p_y$	0	$ba E_r$	$b^2 E_r$	$bc E_r$
$6p_z$	0	$ca E_r$	$cb E_r$	$c^2 E_r$

Planar bismuthene on SiC is believed to be a wide gap 2DTI [25–33]. Several tight-binding models of bismuthene on SiC have been proposed, employing basis sets consisting *only* of the valence orbitals of the bismuth atoms but parameterized to take into account the influence of the SiC substrate on the bismuthene [25,27–32]. For bismuthene on SiC, if the bismuthene lies in the x-y plane, the main contributions to the low energy electronic states are those of the Bi $6p_x$, $6p_y$, and $6s$ atomic valence orbitals [27]; the Bi $6p_z$ valence orbital is shifted away from the Fermi level because of the interaction with the SiC substrate [27]. For this reason most tight-binding models of bismuthene on SiC have employed basis sets consisting of only the Bi $6p_x$, $6p_y$, and $6s$ atomic orbitals. However, in order to treat the nonplanar bismuthene geometry in Fig. 1(b)–1(d), it is necessary to also include the Bi $6p_z$ orbital in the basis.

Thus our basic tight-binding model Hamiltonian is of the form

$$H_{i\alpha s, i'\alpha' s'} = H^{\text{orb}}_{i\alpha, i'\alpha'} \delta_{s,s'} + H^{\text{spin}}_{\alpha s, \alpha' s'} \delta_{i,i'}, \quad (1)$$

where α and α' denote the Bi $6p_x$, $6p_y$, $6p_z$, and $6s$ valence orbitals of atoms i and i', s and s' are spin indices.

$$H^{\text{orb}}_{i\alpha, i'\alpha'} = \left(H^0_{\alpha,\alpha'} + H^C_i \delta_{\alpha,\alpha'}\right)\delta_{i,i'} + H^{\text{hop}}_{i\alpha, i'\alpha'} \quad (2)$$

is the orbital part of the Hamiltonian. $H^0_{\alpha,\alpha'}$ is the site-independent part of the Bi atomic Hamiltonian matrix omitting the spin-orbit and Rashba contributions. H^C_i represents the site-dependence of the electron's Coulomb potential energy. $H^{\text{hop}}_{i\alpha, i'\alpha'}$ is the Hamiltonian matrix element between orbital α' on Bi atom i' and orbital α on Bi atom i.

The on-site orbital matrix elements $H^0_{\alpha,\alpha'}$ are given in Table I. $H^0_{\alpha,\alpha'}$ has energy eigenvalues E_s and E_r corresponding to the orbital states $|6s\rangle$ and $|6p_r\rangle = a|6p_x\rangle + b|6p_y\rangle + c|6p_z\rangle$, respectively, where $\hat{r} = (a, b, c)$ is the unit vector in direction from the nucleus of the Si atom bound to Bi atom i towards the nucleus of Bi atom i. The other two eigenvalues of $H^0_{\alpha,\alpha'}$ correspond to the $6p$ states that are orthogonal to $|6p_r\rangle$ and are both zero. For bismuthene on SiC, $\hat{r}$ is perpendicular to the bismuthene plane and $|6p_r\rangle$ is the $|6p_z\rangle$ orbital. Thus $|6p_r\rangle$, the $6p$ orbital whose symmetry axis is approximately parallel to the local normal to the surface of the cowrie shell-like structure in Figs. 1(b)–1(d), is shifted in energy relative to the other $6p$ orbitals by an amount E_r, emulating the shift of the $6p_z$ orbital relative to $6p_x$ and $6p_y$ for planar bismuthene on SiC [27].

The Hamiltonian matrix elements $H^{\text{hop}}_{i\alpha, i'\alpha'}$ that represent electron hopping between orbital α of Bi atom i and orbital α'

TABLE II. Hamiltonian hopping matrix elements $H_{i\alpha,i'\alpha'}^{\text{hop}}$ in Eq. (2) for interatomic separations $d \leqslant 5.5$ Å. In terms of the coordinates of the primed and unprimed atoms $d = ((x'-x)^2 + (y'-y)^2 + (z'-z)^2)^{\frac{1}{2}}$; $l = (x'-x)/d$; $m = (y'-y)/d$; $n = (z'-z)/d$. Fitting parameter values are $\Sigma = -0.81(1 - 1.532\delta + 0.816\delta^2 - 0.148\delta^3)\,\text{eV}$, $\Sigma' = -0.74(1 - 1.129\delta + 0.442\delta^2 - 0.059\delta^3)\,\text{eV}$, $\Sigma'' = -1.635(1 - 0.612\delta - 0.003\delta^2 + 0.040\delta^3)\,\text{eV}$, $\Pi = 0.407(1 - 1.329\delta + 0.637\delta^2 - 0.107\delta^3)\,\text{eV}$, and $\delta = d - 3.089$ Å.

$H_{i\alpha,i'\alpha'}^{\text{hop}}$	$6s'$	$6p_x'$	$6p_y'$	$6p_z'$
$6s$	Σ	$-\Sigma'l$	$-\Sigma'm$	$-\Sigma'n$
$6p_x$	$\Sigma'l$	$\Sigma''l^2 + \Pi(1-l^2)$	$(\Sigma''-\Pi)lm$	$(\Sigma''-\Pi)ln$
$6p_y$	$\Sigma'm$	$(\Sigma''-\Pi)lm$	$\Sigma''m^2 + \Pi(1-m^2)$	$(\Sigma''-\Pi)mn$
$6p_z$	$\Sigma'n$	$(\Sigma''-\Pi)ln$	$(\Sigma''-\Pi)mn$	$\Sigma''n^2 + \Pi(1-n^2)$

of Bi atom i' are given in Table II for interatomic separations less than or equal to 5.5 Å. They have been fitted to the band structure [27] of planar bismuthene on SiC including nearest-neighbor and second-neighbor hopping. They are assumed to depend on the Bi-Bi bond orientations as in the Slater-Koster model [35] and to scale with the bond lengths as in extended Hückel theory [36]. For interatomic separations greater than 5.5 Å, $H_{i\alpha,i'\alpha'}^{\text{hop}} = 0$. In Eq. (1)

$$H_{\alpha s,\alpha' s'}^{\text{spin}} = H_{\alpha s,\alpha' s'}^{\text{SO}} + H_{\alpha s,\alpha' s'}^{\text{R}}, \tag{3}$$

is the spin-dependent part of the Hamiltonian with H^{SO} the atomic spin-orbit interaction and H^{R} the Rashba Hamiltonian. Following the reasoning in Ref. [27] only the intra-atomic matrix elements of H^{SO} and H^{R} are considered here.

The intra-atomic matrix elements of the spin-orbit Hamiltonian can be approximated as [37,38]

$$H_{\alpha s,\alpha' s'}^{\text{SO}} = \zeta_l \frac{\langle C_\alpha s|\mathbf{S}\cdot\mathbf{L}|C_{\alpha'} s'\rangle}{\hbar^2}, \tag{4}$$

where $\mathbf{S}$ and $\mathbf{L}$ are the spin and orbital angular momentum operators, and C_α is the cubic harmonic that corresponds to orbital state α. ζ_l is the spin-orbit interaction strength and l is the orbital angular momentum quantum number [39]. The matrix $\langle C_\alpha s|\mathbf{S}\cdot\mathbf{L}|C_{\alpha'} s'\rangle/\hbar^2$ is given in Table III. ζ_l is regarded here as a model fitting parameter with value $\zeta_1 = 1.82\,\text{eV}$ for the Bi $6p$ valence orbitals. This value of ζ_1 (obtained by fitting to the band structure of bismuthene on SiC) is consistent with the previous estimate [40] $\zeta_1 \sim 1\,\text{eV}$ of the $6p$-orbital spin-orbit coupling strength for bulk 3D crystalline bismuth, if we consider that in bismuthene on SiC the bismuth $6p$ valence orbitals are strongly perturbed [27] due to bonding between the bismuth atoms and the SiC substrate.

TABLE III. Matrix elements of $\frac{\mathbf{S}\cdot\mathbf{L}}{\hbar^2}$ that enter the intra-atomic spin-orbit Hamiltonian matrix, Eq. (4). All matrix elements involving the atomic s orbital are zero.

$\frac{\langle C_\alpha s|\mathbf{S}\cdot\mathbf{L}|C_{\alpha'} s'\rangle}{\hbar^2}$	$6p_x' \uparrow'$	$6p_x' \downarrow'$	$6p_y' \uparrow'$	$6p_y' \downarrow'$	$6p_z' \uparrow'$	$6p_z' \downarrow'$
$6p_x \uparrow$	0	0	$-i/2$	0	0	$1/2$
$6p_x \downarrow$	0	0	0	$i/2$	$-1/2$	0
$6p_y \uparrow$	$i/2$	0	0	0	0	$-i/2$
$6p_y \downarrow$	0	$-i/2$	0	0	$-i/2$	0
$6p_z \uparrow$	0	$-1/2$	0	$i/2$	0	0
$6p_z \downarrow$	$1/2$	0	$i/2$	0	0	0

Rashba phenomena [41,42] are due to spin-orbit coupling in systems whose symmetry is broken by the presence of a surface or interface. The form of the intra-atomic Rashba Hamiltonian matrix elements $H_{\alpha s,\alpha' s'}^{\text{R}}$ for the present system can be deduced by considering a contribution to $\nabla V(\mathbf{r})$ in the general spin-orbit Hamiltonian [43] $\frac{\hbar}{(2mc)^2}\boldsymbol{\sigma}\cdot\nabla V(\mathbf{r})\times\mathbf{p}$ that we assume to point along the line connecting the nucleus of the Si atom bound to Bi atom i and the nucleus of Bi atom i. The resulting matrix elements are given in Table IV.

For a monolayer of bismuth atoms arranged on the planar honeycomb lattice of bismuthene, the model described by Eq. (1) (with the electron Coulomb potential energy H_i^{C} assumed to be the same for all Bi atoms) provides a good approximation to the known low energy electronic structure of the planar topological insulator monolayer bismuthene on SiC described in Ref. [27]. Specifically, it yields a band structure with a 0.86 eV indirect band gap, the conduction band minimum at the Γ point, the valence band maximum at K, a 0.46 eV Rashba splitting of the valence band maximum and a direct band gap of 1.22 eV at the K point.

In order to tailor our tight-binding model to the cowrie shell-like nanostructure in Figs. 1(b)–1(d) we begin by setting the electron Coulomb potential energy H_i^{C} in Eq. (2) to its values calculated for this system within DFT and compare the electron density of states calculated for the orbital Hamiltonian H^{orb} with the corresponding partial density of states on the bismuth atoms calculated within DFT in the absence of spin-orbit and Rashba effects. The comparison is shown in Fig. 2(a) where the partial density of states (DOS) predicted by DFT is shown in black and the DOS obtained from H^{orb} is in orange. In Fig. 2(a), the 0.325 eV gap between the highest occupied molecular orbital (HOMO) of the cowrie shell-like nanostructure and its lowest unoccupied molecular orbital (LUMO) calculated for the H^{orb} Hamiltonian agrees reasonably well with the 0.36 eV HOMO-LUMO gap predicted by DFT. This is encouraging. However, the gaps between the LUMO and higher energy states, and those between the HOMO and lower energy states, are significantly smaller for the H^{orb} Hamiltonian than those predicted by DFT. We address this discrepancy as follows.

We calculate numerically the eigenvalues ϵ_n and eigenvectors $|n\rangle$ of H^{orb} such that $H^{\text{orb}}|n\rangle = \epsilon_n|n\rangle$ and define a modified orbital Hamiltonian $\tilde{H}^{\text{orb}}$ by its matrix elements in the basis of valence orbitals of the Bi atoms as

$$\tilde{H}_{i\alpha,i'\alpha'}^{\text{orb}} = \sum_n \langle i\alpha|n\rangle(\epsilon_n + \gamma_n)\langle n|i'\alpha'\rangle, \tag{5}$$

TABLE IV. Matrix elements of the intra-atomic Rashba Hamiltonian H^R, Eq. (3). Here $\hat{r} = (a, b, c)$ is the unit vector in direction from the nucleus of the Si atom bound to Bi atom i towards the nucleus of Bi atom i. The fitting parameter value is $R = 0.56$ eV.

$H^R_{\alpha s, \alpha' s'}$	$6s' \uparrow'$	$6s' \downarrow'$	$6p'_x \uparrow'$	$6p'_x \downarrow'$	$6p'_y \uparrow'$	$6p'_y \downarrow'$	$6p'_z \uparrow'$	$6p'_z \downarrow'$
$6s \uparrow$	0	0	$-iRb$	Rc	iRa	$-iRc$	0	$iR(b + ia)$
$6s \downarrow$	0	0	$-Rc$	iRb	$-iRc$	$-iRa$	$iR(b - ia)$	0
$6p_x \uparrow$	iRb	$-Rc$	0	0	0	0	0	0
$6p_x \downarrow$	Rc	$-iRb$	0	0	0	0	0	0
$6p_y \uparrow$	$-iRa$	iRc	0	0	0	0	0	0
$6p_y \downarrow$	iRc	iRa	0	0	0	0	0	0
$6p_z \uparrow$	0	$-iR(b + ia)$	0	0	0	0	0	0
$6p_z \downarrow$	$-iR(b - ia)$	0	0	0	0	0	0	0

where α and α' denote the Bi $6p_x$, $6p_y$, $6p_z$, and $6s$ valence orbitals of atoms i and i'. If $\gamma_n = 0$ for all n, $\tilde{H}^{orb}$ reduces to H^{orb}. However, by choosing the values of γ_n appropriately we are able to bring the density of states calculated for the modified orbital Hamiltonian $\tilde{H}^{orb}$ [shown in orange in Fig. 2(b)] into excellent agreement at low and moderate energies with the density of states calculated within DFT [shown in black

FIG. 2. (a) Partial density of states (DOS) projected on the bismuth atoms of the structure in Fig. 1(b)–1(d) that is predicted by DFT is shown in black and the DOS obtained from the orbital Hamiltonian H^{orb} is in orange. (b) DOS predicted by DFT is shown in black and the DOS obtained from the modified orbital Hamiltonian $\tilde{H}^{orb}$ is in orange.

in Fig. 2(b)]. The values of γ_n that yield this agreement are shown in Table V. Our optimized tight-binding model is then

$$\tilde{H}_{i\alpha s, i'\alpha' s'} = \tilde{H}^{orb}_{i\alpha, i'\alpha'} \delta_{s,s'} + H^{spin}_{\alpha s, \alpha' s'} \delta_{i,i'}, \qquad (6)$$

where H^{spin} is given by Eq. (3).

III. SPIN FILTERING FORMALISM

Within the Landauer formalism [44,45] the two-terminal source-drain conductance G of a nanostructure at zero temperature in the linear response regime is given by

$$G = \frac{e^2}{h} T(E_F), \qquad (7)$$

where the electron transmission probability through the nanostructure at energy E is

$$T(E) = \sum_{\alpha, s, i, \beta, s', j} |t_{\beta, s', j, \alpha, s, i}(E)|^2 \frac{v_{\beta, s', j}}{v_{\alpha, s, i}}. \qquad (8)$$

Here $t_{\beta, s', j, \alpha, s, i}$ is the amplitude for electron scattering at the Fermi energy from state α with spin s of 1D lead i connected to the electron source to state β with spin s' of 1D lead j connected to the electron drain reservoir. $v_{\alpha, s, i}$ and $v_{\beta, s', j}$ are the corresponding subband Fermi velocities.

Here we shall apply this formalism to study spin filtering by the cowrie shell-like nanostructure shown in Figs. 1(b)–1(d), described by the optimized model Hamiltonian $\tilde{H}$ given by Eq. (6). We consider spin-unpolarized electrons entering the device through the electron source contact and calculate the spin resolved probabilities $T_\uparrow$ and $T_\downarrow$ of spin-up and spin-down electrons exiting through the drain contact at energy E. $T_\uparrow$ and $T_\downarrow$ are obtained by restricting the sum over s' in Eq. (8) to spin-up and spin-down states, respectively, while including both the spin-up and spin-down states in the sum over s. We then define the spin polarization of the electrons entering the drain electrode as

$$P = T_\uparrow / (T_\uparrow + T_\downarrow). \qquad (9)$$

TABLE V. Values of γ_n in Eq. (5) that yield the DOS shown in orange in Fig. 2(b). States numbered n are counted from the HOMO level ($n = 0$). The LUMO is $n = 1$. Spin up and down are not counted separately.

n	$\leqslant -7$	-6	-5	-4	-3	-2	-1	0	1	2	3	4	5	6	$\geqslant 7$
γ_n (eV)	-0.370	-0.3774	-0.4596	-0.450	-0.4346	-0.5204	-0.376	0.00	0.04	0.30	0.367	0.30	0.26	0.26	0.30

Importantly, in order for this definition to represent the physical spin polarization that is the figure of merit for spin filters, we choose the direction of the axis of quantization for electron spin states in the drain electrode to be the direction of the expectation value of the spin vector of the electrons carrying the the electric current in the drain. Within Landauer theory, this direction is the direction of the vector

$$\mathbf{S} = \frac{1}{N} \sum_{\alpha,s,i,\beta,s',j} |t_{\beta,s',j,\alpha,s,i}(E)|^2 \langle \beta, s', j|\hat{\mathbf{S}}|\beta, s', j\rangle \frac{v_{\beta,s',j}}{v_{\alpha,s,i}},$$
(10)

where $\hat{\mathbf{S}} = \frac{\hbar}{2}\vec{\sigma}$, $\vec{\sigma} = (\sigma_x, \sigma_y, \sigma_z)$ are the Pauli matrices, N is a normalization factor, and the remaining symbols in Eq. (10) are as in Eq. (8).

We calculate $\mathbf{S}$ numerically and then set the direction of the spin quantization axis for the drain to be the direction of $\mathbf{S}$ for each configuration of source and drain electrodes and for each value of the electron energy under consideration.

The scattering amplitudes $t_{\beta,s',j,\alpha,s,i}$ are obtained by solving numerically the Lippmann-Schwinger equation

$$|\psi\rangle = |\phi_\circ^{\alpha,s,i}\rangle + G_\circ(E)V|\psi\rangle.$$
(11)

Here $|\phi_\circ^{\alpha,s,i}\rangle$ is an eigenstate of the ith ideal 1D lead that is decoupled from the nanostructure consisting of the quantum dot and conducting contacts (if those are present), $G_\circ(E)$ is the sum of the Green's functions of the nanostructure and 1D leads if they are decoupled from the nanostructure, and $|\psi\rangle$ is the corresponding exact scattering eigenstate of the coupled system. V is the coupling Hamiltonian between the nanostructure and the ideal 1D leads. A methodology for numerically solving Lippmann-Schwinger equations such as Eq. (11) within a tight-binding framework is described in Appendix A of Ref. [46].

In the present paper the ideal leads are represented by 1D tight-binding chains. Each site of each chain is assumed to have 6 orbitals, including spin. The on-site energies of these chain orbitals are the same as the corresponding atomic orbital energies $\tilde{H}_{i\alpha s, i\alpha s}$ of the $6p_x, 6p_y$, and $6p_z$ orbitals of the Bi atoms described by the Hamiltonian Eq. (6). Only nearest-neighbor Hamiltonian matrix elements *between like orbitals* of the 1D chains and between the chains and adjacent Bi atoms of the nanostructure are assumed to be nonzero. For simplicity, all of these nearest-neighbor Hamiltonian matrix elements are assumed to have the same value $t = -2.0\,\text{eV}$.

IV. RESONANT AND NONRESONANT SPIN FILTERING

The spin filtering that we find (including both its effectiveness and the underlying mechanism) depends strongly on which atoms of the cowrie shell-like nanostructure serve as contacts for the source and drain leads, as is demonstrated in Fig. 3. (We note in passing that making electrical contact to individual atoms is feasible at the present time with the help of scanning tunneling microscope tips [47] or nanoscale mechanical break junctions [48].)

The black curve in Fig. 3(a) shows the spin polarization $P = T_\uparrow/(T_\uparrow + T_\downarrow)$ of electrons entering the drain (connected to the Bi atom colored pale blue in the inset) after spin-unpolarized electrons enter the nanostructure at energy E from the source that is connected to the chartreuse Bi atom
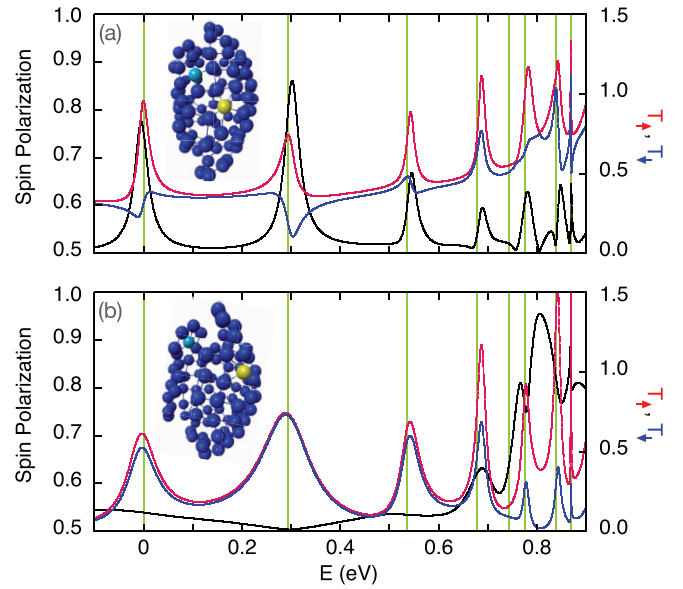
FIG. 3. [(a), (b)] Spin filtering by the nanostructure shown in Figs. 1(b)–1(d) for two different arrangements of the source and drain contacts. The graphs present the calculated spin-resolved Landauer transmission probabilities $T_\uparrow$ (red) and $T_\downarrow$ (blue) of spin-up and spin-down electrons exiting from the nanostructure into the drain contact at energy E and the corresponding spin polarization $P = T_\uparrow/(T_\uparrow + T_\downarrow)$ (black). The electron energy is measured from the Fermi level. The green vertical lines indicate the energy eigenvalues of the optimized tight-binding Hamiltonian $\tilde{H}$, Eq. (6). It is assumed that spin-unpolarized electrons enter the nanostructure from the electron source. Insets show only the bismuth atoms of the nanostructure and indicate the atoms (colored chartreuse and pale blue, respectively) to which the source and drain contacts are attached in parts (a) and (b).

in the inset. The spin-resolved Landauer transmission probabilities $T_\uparrow$ and $T_\downarrow$ of spin-up and spin-down electrons are shown in red and blue, respectively. The peaks of the spin polarization in Fig. 3(a) closely match the energy eigenvalues of the optimized tight-binding Hamiltonian $\tilde{H}$, Eq. (6), that are indicated by green vertical lines. Consequently the spin filtering mechanism in Fig. 3(a) is spin-dependent resonant scattering of electrons through the nanostructure.

The physics of the resonant spin filtering is as follows: When the energy of electrons transmitted through the cowrie shell-like nanostructure is close to an energy eigenvalue that corresponds to an eigenstate of the Hamiltonian $\tilde{H}$ of the isolated nanostructure, both electron forward scattering through the nanostructure and electron backscattering from the nanostructure occur partly via that eigenstate. This can result in a peak or dip (known as a resonance or antiresonance, respectively) in the electron transmission probability through the nanostructure as a function of the electron energy. In a system with strong spin-orbit coupling (such as the present one) the electron transmission probabilities via the Hamiltonian eigenstates can differ for spin-up and spin-down electrons and can also depend strongly on the details of how the electron source and drain leads couple to eigenstates of the nanostructure's Hamiltonian. At electron energies where the transmission of one spin species is enhanced and that of the other spin species

is suppressed due to scattering via an eigenstate or eigenstates of the nanostructure's Hamiltonian resonant spin filtering occurs.

Notice that while the spin-up transmission probability $T_\uparrow$ [the red curve in Fig. 3(a)] displays either a peak (or no discernible feature) at *every* energy eigenvalue of $\tilde{H}$, $T_\downarrow$ (the blue curve) displays a resonant peak at some eigenvalues of $\tilde{H}$ and an antiresonant dip at others. [The origin of this apparent asymmetry between spin up and spin down is our choice of the direction of the axis of spin quantization being the *same* as the direction of the expectation value of the spin vector of the electrons transmitted into the drain electrode at each energy; see Eq. (10).] Where the resonant peak in $T_\uparrow$ coincides with a particularly strong antiresonant dip in $T_\downarrow$ the value of the spin polarization $P = T_\uparrow/(T_\uparrow + T_\downarrow)$ is enhanced and spin filtering is especially effective. Thus near $E = 0.3$ eV in Fig. 3(a) the maximum spin-polarization value ($P = 0.861$) exceeds that of the other spin-polarization maxima, even where $T_\uparrow$ is *larger* than near $E = 0.3$ eV, because $T_\downarrow$ has its deepest minimum near $E = 0.3$ eV.

In Fig. 3(b) we show the results of our spin transport calculations for a different choice of the bismuth atoms to which the source and drain leads are attached, as depicted in the inset of Fig. 3(b). The spin filtering behavior in Fig. 3(b) differs markedly from that in Fig. 3(a): In Fig. 3(b) the coupling of the leads to the resonant states of the nanostructure is very different than in Fig. 3(a). Because of this, $T_\downarrow$ displays only resonant peaks (no antiresonant dips). Also the resonances near $E = 0, 0.3$ and 0.54 eV are much broader than in Fig. 3(a) and the values of $T_\uparrow$ and $T_\downarrow$ are almost equal for those resonances. This results in much weaker resonant spin filtering than in Fig. 3(a) at most resonant energies.

However, a very strong spin filtering peak (spin polarization P as large as 0.956) can be seen in Fig. 3(b) near $E = 0.8$ eV, in between two adjacent energy eigenvalues of $\tilde{H}$. This peak coincides with minima of *both* $T_\uparrow$ and $T_\downarrow$. It is clearly not a resonant phenomenon since it occurs *between* two energy eigenvalues $\tilde{H}$. Instead it is due to especially weak nonresonant down-spin transmission with $T_\downarrow$ as low as 0.018. This nonresonant spin scattering asymmetry is also due to the strong spin-orbit coupling in the present system.

Finally, we note that in both Figs. 3(a) and 3(b) the source and drain leads are attached to bismuth atoms that each have more than three nearest neighbors, and in each case one or both of these atoms is not located at a residual edge of the bismuthene that can be discerned in Fig. 1(b). Thus we believe that the spin filtering mechanisms described above differ fundamentally from edge-state phenomena.

This conclusion is supported by the results shown in Fig. 4, where the electron populations induced in linear response on the Bi atoms of the cowrie shell-like nanostructure by the electron source to drain current are shown in gray scale. The highest (lowest) induced populations are black (palest gray). The source and drain contacts are attached to the Bi atoms colored chartreuse and pale blue, respectively. The source and drain atoms in Figs. 4(a) and 4(b) are the same as in Figs. 3(a) and 3(b), respectively. In Fig. 4(a) the Fermi level is at 0.303 eV where the strongest resonant spin filtering is seen in Fig. 3(a). In Fig. 4(b) the Fermi level is at 0.807 eV where the strongest nonresonant spin filtering is seen in Fig. 3(b).
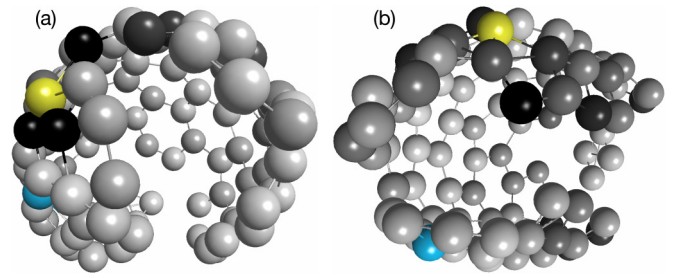
FIG. 4. Electron populations induced on the Bi atoms of the cowrie shell-like nanostructure by the electron source to drain current in linear response, represented in gray scale. The Bi atoms with the largest (smallest) induced electron populations are shown in black (palest gray). The source and drain contacts are attached to the Bi atoms colored chartreuse and pale blue, respectively. In (a) and (b) the leads are attached to the same atoms as in Figs. 3(a) and 3(b), respectively. (a) Electron Fermi level at 0.303 eV, the center of the strongest resonant spin polarization peak in Fig. 3(a). (b) Electron Fermi level at 0.807 eV, the center of the strongest nonresonant spin polarization peak shown in Fig. 3(b). Image prepared using Macmolplt software [34].

The electron populations in Fig. 4 differ strikingly from those of edge states of topological insulators: Topological insulator edge states are localized near the edge of a sample and extend along the *entire* edge since they propagate along the edge without back scattering [10]. By contrast, in Fig. 4 the large current-induced electron populations (shown in black) are mainly localized to the vicinities of the (chartreuse) electron source atoms; they do not extend far along the edge of the cowrie shell. Thus the edge-state paradigm does not account for the strong resonant and nonresonant spin filtering seen in Fig. 3. Instead, the distributions of the current-induced electron populations over the cowrie shell in Fig. 4 are suggestive of localized electronic states associated with strong disorder. The electron populations are large in the vicinity of the electron source electrode (the chartreuse colored atom) and decay at larger distances from the source electrode, reaching the drain electrode (the pale blue atom) with a low amplitude. Indeed, as we have discussed in Sec. I, *strong* structural disorder is present in the cowrie shell-like nanostructure in the form of large variations of the Bi-Bi bond lengths and variable Bi atomic coordination numbers, especially at and near the the edge of the cowrie shell, lending credence to this physical interpretation of Fig. 4 and also accounting for the breakdown of the edge-state paradigm in this system. As a check, we have also explicitly calculated the electron populations of the eigenstates of the cowrie shell Hamiltonian [Eq. (6)] that are closest in energy to the strongest spin filtering features of Figs. 3(a) and 3(b) and found them to be localized near the source electrode similarly to the electron populations in Fig. 4. Thus we are led to propose that the strong resonant and nonresonant spin filtering that we have found in the cowrie shell-like nanostructure is due to the combination of localization of electronic states associated with strong structural disorder and strong spin-orbit coupling.

It follows from the above discussion that the *details* of the structure of the eigenstates of the electronic Hamiltonian of this strongly disordered system and of their coupling to

the source and drain leads determine whether or not there is strong spin filtering for leads connected to any particular pair of Bi atoms. In this paper we have presented results for two representative choices of the atoms connected to the source and drain leads for which there is strong spin filtering. Our simulations have shown that some other choices of the source and drain lead atoms also result in strong spin filtering while still other choices do not. Since the details of the electronic quantum eigenstates of this disordered system and of their coupling to the leads determine whether strong spin filtering occurs or does not occur, only a quantum transport calculation can predict whether any given choice of source and drain lead atoms should support strong spin filtering.

V. SUMMARY

Previous work has predicted [11] that a hemispherical bismuthene dome with an zigzag edge can be stabilized by a silicon adsorbate and can be made into an effective two-terminal spin filter by virtue of its spin-polarized edge states. Here we have shown theoretically that similar bismuthene-silicon domes, but with armchair edges, are, by contrast, unstable and fold spontaneously into stable cowrie shell-like nanostructures. The calculations that we have presented predict that these nanostructures should display two distinct strong spin filtering mechanisms at zero magnetic field. These mechanisms should manifest for different arrangements of source and drain leads attached to the nanostructure. One of these mechanisms is resonant spin filtering where a peak in resonant transmission of one spin species through the nanostructure coincides with an antiresonant transmission dip for the other spin species. The second mechanism is strong nonresonant spin filtering where nonresonant transmission of one spin species is much weaker than that of the other spin species. These spin filtering mechanisms arise from localized electronic states associated with strong disorder and strong spin-orbit coupling in bismuthene and differ fundamentally from edge state-related spin filtering mechanisms and the spin Hall effect.

ACKNOWLEDGMENTS

[1] C. L. Kane and E. J. Mele, Quantum Spin Hall Effect in Graphene, Phys. Rev. Lett. **95**, 226801 (2005).

[2] C. L. Kane and E. J. Mele, Z_2 Topological Order and the Quantum Spin Hall Effect, Phys. Rev. Lett. **95**, 146802 (2005).

[3] B. A. Bernevig, T. L. Hughes, and S.-C. Zhang, Quantum spin Hall effect and topological phase transition in HgTe quantum wells, Science **314**, 1757 (2006).

[4] L. Fu and C. L. Kane, Topological insulators with inversion symmetry, Phys. Rev. B **76**, 045302 (2007).

[5] M. König, S. Wiedmann, C. Brüne, A. Roth, H. Buhmann, L. W. Molenkamp, X. L. Qi, and S. C. Zhang, Quantum spin Hall insulator state in HgTe quantum wells, Science **318**, 766 (2007).

[6] J. E. Moore and L. Balents, Topological invariants of time-reversal-invariant band structures, Phys. Rev. B **75**, 121306(R) (2007).

[7] M. Z. Hasan and C. L. Kane, Colloquium: Topological insulators, Rev. Mod. Phys. **82**, 3045 (2010).

[8] X.-L. Qi and S.-C. Zhang, Topological insulators and superconductors, Rev. Mod. Phys. **83**, 1057 (2011).

[9] Y. Ando, Topological insulator materials, J. Phys. Soc. Jpn. **82**, 102001 (2013)

[10] J. K. Asbóth, L. Oroszlány, and A. Pályi, *A Short Course on Topological Insulators*, Lectre Notes in Physics, Sec. 8.4, Vol. 919 (Springer, New York, 2016).

[11] A. Saffarzadeh and G. Kirczenow, Nearly perfect spin filtering in curved two-dimensional topological insulators, Phys. Rev. B **102**, 235420 (2020).

[12] M. J. Frisch, G. W. Trucks, H. B. Schlegel, G. E. Scuseria, M. A. Robb, J. R. Cheeseman, G. Scalmani, V. Barone, G. A. Petersson *et al.*, The GAUSSIAN 16 Revision: A.03 computer code was used.

[13] R. Tenne, Advances in the synthesis of inorganic nanotubes and fullerene-like nanoparticles, Angew. Chem. Int. Ed. **42**, 5124 (2003).

[14] Y. Li, J. Wang, Z. Deng, Y. Wu, X. Sun, D. Yu, and P. Yang, Bismuth nanotubes: A rational low-temperature synthetic route, J. Am. Chem. Soc. **123**, 9904 (2001).

[15] B. Yang, C. Li, H. Hu, X. Yang, Q. Li, and Y. Qian, A room-temperature route to bismuth nanotube arrays, Eur. J. Inorg. Chem. **2003**, 3699 (2003).

[16] L. Li, Y. W. Yang, X. H. Huang, G. H. Li, R. Ang, and L. D. Zhang, Fabrication and electronic transport properties of Bi nanotube arrays, Appl. Phys. Lett. **88**, 103119 (2006).

[17] D. Yang, G. Meng, Q. Xu, F. Han, M. Kong, and L. Zhang, Electronic transport behavior of bismuth nanotubes with a pre-designed wall thickness, J. Phys. Chem. C **112**, 8614 (2008).

[18] D. Ma, J. Zhao, Y. Li, X. Su, S. Hou, Y. Zhao, X. Hao, and L. Li, Organic molecule directed synthesis of bismuth nanostructures with varied shapes in aqueous solution and their optical characterization, Colloids Surf. A **368**, 105 (2010).

[19] S. Derrouiche, C. Z. Loebick, and L. Pfefferle, Optimization of routes for the synthesis of bismuth nanotubes: Implications for nanostructure form and selectivity, J. Phys. Chem. C **114**, 3431 (2010).

[20] S. Derrouiche, C. Z. Loebick, C. Wang, and L. Pfefferle, Energy-induced morphology changes in bismuth nanotubes, J. Phys. Chem. C **114**, 4336 (2010).

[21] R. Boldt, M. Kaiser, D. Kšhler, F. Krumeich, and M. Ruck, High-yield synthesis and structure of double-walled bismuth-nanotubes, Nano Lett. **10**, 208 (2010).

[22] J. Tillmann, J. H. Wender, U. Bahr, M. Bolte, H.-W. Lerner, M. C. Holthausen, and M. Wagner, One-step synthesis of a [20]silafullerane with an endohedral chloride ion, Angew. Chem. Int. Ed. **54**, 5429 (2015).

[23] A. N. Thiessen, M. Ha, R. W. Hooper, H. Yu, A. O. Oliynyk, J. G. C. Veinot, and V. K. Michaelis, Silicon nanoparticles: Are they crystalline from the core to the surface? Chem. Mater. **31**, 678 (2019).

[24] C.-C. Huang, Y. Tang, M. van der Laan, J. van de Groep, A. F. Koenderink, and K. Dohnalova, Band-gap tunability in partially amorphous silicon nanoparticles using single-dot correlative microscopy, ACS Appl. Nano Mater. **4**, 288 (2021).

[25] G. Kirczenow, Perfect and imperfect conductance quantization and transport resonances of two-dimensional topological-insulator quantum dots with normal conducting leads and contacts, Phys. Rev. B **98**, 165430 (2018).

[26] C.-H. Hsu, Z.-Q. Huang, F.-C. Chuang, C.-C. Kuo, Y.-T. Liu, H. Lin, and A. Bansil, The nontrivial electronic structure of Bi/Sb honeycombs on SiC(0001), New J. Phys. **17**, 025005 (2015).

[27] F. Reis, G. Li, L. Dudy, M. Bauernfeind, S. Glass, W. Hanke, R. Thomale, J. Schäfer, and R. Claessen, Bismuthene on a SiC substrate: A candidate for a high-temperature quantum spin Hall material, Science **357**, 287 (2017).

[28] F. Dominguez, B. Scharf, G. Li, J. Schäfer, R. Claessen, W. Hanke, R. Thomale, and E. M. Hankiewicz, Testing topological protection of edge states in hexagonal quantum spin Hall candidate materials, Phys. Rev. B **98**, 161407(R) (2018).

[29] G. Li, W. Hanke, E. M. Hankiewicz, F. Reis, J. Schäfer, R. Claessen, C. Wu, and R. Thomale, Theoretical paradigm for the quantum spin Hall effect at high temperatures, Phys. Rev. B **98**, 165146 (2018).

[30] L. M. Canonico, T. G. Rappoport, and R. B. Muniz, Spin and Charge Transport of Multiorbital Quantum Spin Hall Insulators, Phys. Rev. Lett. **122**, 196601 (2019).

[31] M. Azari and G. Kirczenow, Valley polarization reversal and spin ferromagnetism and antiferromagnetism in quantum dots of the topological insulator monolayer bismuthene on SiC, Phys. Rev. B **100**, 165417 (2019).

[32] X. Hao, F. Luo, S. Zhai, Q. Meng, J. Wu, L. Zhang, T. Li, Y. Jia, and M. Zhou, Strain-engineered electronic and topological properties of bismuthene on SiC(0001) substrate, Nano Futures **3**, 045002 (2019).

[33] R. Stühler, F. Reis, T. Mller, T. Helbig, T. Schwemmer, R. Thomale, J. Schäfer, and R. Claessen, Tomonaga-Luttinger liquid in the edge channels of a quantum spin Hall insulator, Nat. Phys. **16**, 47 (2020).

[34] B. M. Bode and M. S. Gordon, Macmolplt: A graphical user interface for GAMESS, J. Mol. Graph. Model. **16**, 133 (1998).

[35] J. C. Slater and G. F. Koster, Simplified LCAO method for the periodic potential problem, Phys. Rev. **94**, 1498 (1954).

[36] J. H. Ammeter, H. B. Buergi, J. C. Thibeault, and R. Hoffmann, Counterintuitive orbital mixing in semiempirical and ab initio molecular orbital calculations, J. Am. Chem. Soc. **100**, 3686 (1978).

[37] F. Rostamzadeh Renani and G. Kirczenow, Ligand-based transport resonances of single-molecule-magnet spin filters: Suppression of Coulomb blockade and determination of easy-axis orientation, Phys. Rev. B **84**, 180408(R) (2011).

[38] F. Rostamzadeh Renani and G. Kirczenow, Tight binding model of Mn$_{12}$ single molecule magnets: Electronic and magnetic structure and transport properties, Phys. Rev. B **85**, 245415 (2012).

[39] E. U. Condon and G. H. Shortley, *The Theory of Atomic Spectra* (Cambridge University Press, London, 1935).

[40] Y. Liu and R. E. Allen, Electronic structure of the semimetals Bi and Sb, Phys. Rev. B **52**, 1566 (1995).

[41] Y. A. Bychkov and E. I. Rashba, Properties of a 2D electron gas with lifted spectral degeneracy, Pis'ma Zh. Eksp. Teor. Fiz. **39**, 66 (1984) [Properties of a 2D electron gas with lifted spectral degeneracy, JETP Lett. **39**, 78 (1984)].

[42] Y. A. Bychkov and E. I. Rashba, Oscillatory effects and the magnetic susceptibility of carriers in inversion layers, J. Phys. C **17**, 6039 (1984).

[43] C. Kittel, *Quantum Theory of Solids* (Wiley, New York, 1963), p. 181.

[44] E. N. Economou and C. M. Soukoulis, Static Conductance and Scaling Theory of Localization in One Dimension, Phys. Rev. Lett. **46**, 618 (1981).

[45] D. S. Fisher and P. A. Lee, Relation between conductivity and transmission matrix, Phys. Rev. B **23**, 6851 (1981).

[46] M. Azari and G. Kirczenow, Gate-tunable valley currents, non-local resistances and valley accumulation in bilayer graphene nanostructures, Phys. Rev. B **95**, 195424 (2017).

[47] M. F. Crommie, C. P. Lutz, and D. M. Eigler, Confinement of electrons to quantum corrals on a metal surface, Science **262**, 218 (1993).

[48] M. A. Reed, C. Zhou, C. J. Muller, T. P. Burgin, and J. M. Tour, Conductance of a molecular junction, Science **278**, 252 (1997).